

See discussions, stats, and author profiles for this publication at: <https://www.researchgate.net/publication/249315274>

A Molecular Dynamics Study of the Role of Adatoms in SAMs of Methylthiolate on Au(111): A New Force Field Parameterized from Ab Initio Calculations

ARTICLE *in* THE JOURNAL OF PHYSICAL CHEMISTRY C · JUNE 2012

Impact Factor: 4.77 · DOI: 10.1021/jp301378x

CITATIONS

6

READS

31

3 AUTHORS, INCLUDING:



Gabriel S Longo

National Scientific and Technical Research Co...

24 PUBLICATIONS 218 CITATIONS

SEE PROFILE



Somesh Kr. Bhattacharya

Kyoto University

12 PUBLICATIONS 93 CITATIONS

SEE PROFILE

A Molecular Dynamics Study of the Role of Adatoms in SAMs of Methylthiolate on Au(111): A New Force Field Parameterized from Ab Initio Calculations

Gabriel S. Longo,^{*,†} Somesh Kr. Bhattacharya,[‡] and Sandro Scandolo^{*,‡,§}

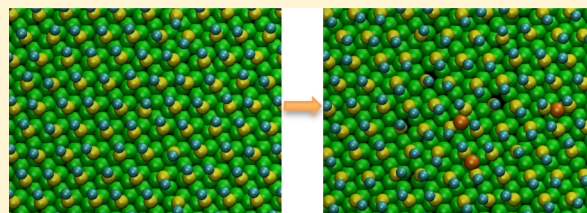
[†]Department of Materials Science and Engineering, Northwestern University, 2220 Campus Drive, Evanston, Illinois 60208, United States

[‡]The Abdus Salam International Center for Theoretical Physics, Strada Costiera 11, 34151 Trieste, Italy

[§]INFN/DEMOCRITOS National Simulation Center, Via Beirut 2-4, I-34014, Trieste, Italy

Supporting Information

ABSTRACT: Starting from ab initio calculations and using a force matching procedure, we have developed a new force field for molecular dynamics simulations of self-assembled monolayers of methylthiolate (MT) on Au(111) surfaces. This new force field is able to reproduce several observed features of SAMs of MT on Au(111) surface, such as the formation of gold vacancy islands and the $(\sqrt{3} \times \sqrt{3})R30$ lattice. We have studied the dynamics of Au adatoms and monatomic vacancies on the Au(111) surface for the SAM of MT at room temperature. It is observed that monatomic vacancies coarsen to form large vacancy islands while the adatoms group to form clusters. Both results are in agreement with experiments. At elevated temperatures, Au adatoms that are lifted from the surface leave an atomic vacancy on it. The liquid-like diffusion of gold adatoms on the SAM surface occurs by hopping between pairs of methylthiolate to which the adatom is temporarily bound. Our findings indicate that structural models of the $c(4 \times 2)$ unit cell including adatoms and vacancies at room temperature need to be revisited.



1. INTRODUCTION

Self-assembled monolayers (SAMs) are extensively studied in nanoscience and surface science due to their broad range of potential applications that include biosensing,¹ nanotechnology² and molecular electronics.³ The most widely used SAMs are those of alkanethiols adsorbed on metallic surfaces, particularly on the (111) surface of gold.^{4–6} The strong thiol–gold surface bond provides a high degree of stability to the layer as well as controllable surface chemical functionality, while the packed alkane chains supply an ordered membrane-like environment that can be useful for bioapplications.

Scanning tunneling microscope (STM)^{7–10} and atomic force microscope (AFM)¹¹ experiments of alkanethiol SAMs on Au(111) at saturation coverage ($\theta = 1/3$ ML) have revealed a simple hexagonal $(\sqrt{3} \times \sqrt{3})R30$ (hereafter denoted as $\sqrt{3}$) surface unit cell that contains a single thiol molecule. Subsequent studies showed the additional presence of a $c(4 \times 2)$ unit cell, which is a superlattice of the $\sqrt{3}$ unit cell containing four thiol molecules, in the 2D structure of alkanethiol SAMs. Such unit cell was found by low energy atom diffraction (LEAD),^{12,13} STM^{4,14} and grazing incidence X-ray diffraction (GIXRD)¹⁵ experiments. In particular, a $c(4 \times 2)$ unit cell of methylthiolate (MT) SAMs on Au(111) at saturation coverage and room temperature was observed by LEAD¹⁶ and STM,¹⁷ which suggests that the interaction between sulfur (S) and gold plays a very important role in determining the structure of the surface since the patterns

found for larger alkanethiols are also observed for MT, the shortest one.

More recently, STM images showed the involvement of gold adatoms in the binding of methylthiols to the Au(111) surface at low coverage and low temperature.¹⁸ The authors suggested that the reconstruction of the herringbone surface was the source of the gold adatoms, which are the driving force of methylthiolate self-assembly. Thus, surface gold adatoms might be involved in the $c(4 \times 2)$ unit cell observed for MT–Au(111) SAMs. This was also suggested by the density functional theory (DFT) study of Grönbeck et al.,¹⁹ where a unit cell containing two adatoms was proposed. Further evidence in support of the inclusion of adatoms to describe the $c(4 \times 2)$ lattice of the MT–Au(111) surface was given by Mazzarello et al.²⁰ DFT molecular dynamics (MD) simulations^{20,21} have shown that adatoms are generated from the top layer of the Au(111) surface leaving an atomic vacancy in the topmost substrate layer. These MD simulations also suggest a dynamic equilibrium between the bridge site adsorption and a novel structure where two MT radicals are bonded to a Au adatom. Such adatoms and vacancies result in a large surface roughness, which was confirmed by photoelectron and GIXRD measurements. Ab initio calculations have also shown the model of the

Received: February 10, 2012

Revised: June 13, 2012

Published: June 19, 2012

$c(4 \times 2)$ unit cell of the MT–Au(111) surface, at saturation coverage, containing one Au vacancy and one Au adatom to be energetically favorable.^{20,22}

Furthermore, atomic gold vacancies in the upper gold layer were previously suggested to stabilize the $\sqrt{3}$ lattice of methylthiolate on Au(111) using DFT.²³ Recently, Torres et al.²⁴ have also found a $c(4 \times 2)$ unit cell with two gold adatoms and no vacancy to be energetically favorable for 1/3 ML of ethylthiol on gold(111). The authors suggested that the Au adatoms are lifted from the surface leaving an atomic vacancy, which in a later stage diffuses to the domain's boundary, which explains the formation of gold vacancy islands that are typically observed in high density alkanethiol SAMs. In this regard, gold vacancy islands, which are one of the most prominent features of SAMs of alkanethiols, are single-atom height defects in the Au(111) layer.^{14,25,26} STM experiments^{17,27} have suggested that these islands are formed during alkanethiol adsorption by an excess of Au adatoms due to the relaxation of the Au(111) herringbone reconstruction. At saturation coverage of the alkanethiol SAM, gold vacancy islands are uniformly covered by the adsorbates.²⁸

In summary, there is a vast range of evidence suggesting the involvement of gold vacancies and adatoms in the observed behavior of SAMs of thiols on gold. However, the understanding of the extent of such involvement is still far from being complete. Till date several groups have performed MD simulations of alkanethiol SAMs on a gold surface^{29–36} including MD simulations with ab initio based force fields.^{31,32,34–37} However, none of these addressed the presence of surface defects. Olmos-Asar et al.³⁷ included adatom configurations in the fitting of their semiempirical thiol-gold potential, but they did not apply it to study the behavior of adatoms on the SAM surface. Moreover, the DFT simulations which successfully grab the defects on the surface were performed for smaller systems (~ 40 – 50 atoms) and for short time scale (\sim picoseconds). Consequently, there is a need to perform MD simulations for larger systems and on a longer time scale. We, therefore, resort to classical MD simulations with a force field capable of reproducing the experimental and DFT results. We developed our own force field starting from ab initio calculations and performing a force matching procedure. Using this force field, we perform MD simulations to investigate the role of gold adatoms and vacancies in determining the structure of methylthiolate SAMs on Au(111). The main goal of this work is to model the dynamical behavior of gold atoms in such monolayers.

This paper is organized as follows: in the next section, we describe the force matching procedure used to parametrize our force field, present the technical details of the MD simulations, and characterize the potential energy landscape and the resulting surface structures of our approach. In section 3, we discuss the simulation results obtained using such parametrization, with particular emphasis on the dynamic role of surface gold atoms in SAMs of methylthiolates on Au(111). In the last section, we summarize our results and discuss directions for future work.

2. METHODOLOGY

In this section, we first describe the functional form and parametrization of the potentials used in the MD simulations, followed by giving the details of such simulations. Then, we describe the potential energy landscape of our force field, which matches with previous DFT results. Finally, we present the

calculated structures of Au(111) and MT–Au(111) surfaces using our force field.

2.1. Force Field Parametrization: Force Matching. The MT–Au(111) force field is constructed from first-principle calculations using the force-matching method,³⁸ where the classical MD potentials are obtained by fitting the ab initio atomic forces of many different configurations of the system. Examples of applications of this general technique include potentials for aluminum³⁸ and liquid silica³⁹ developed from ab initio calculations, potentials for water⁴⁰ and ionic liquids⁴¹ obtained from ab initio MD trajectories, and coarse-grained force fields for biomolecular systems parametrized from fully atomistic classical MD trajectories.⁴²

The input configurations that have been used in this study to perform the force matching were taken from the Car–Parrinello MD⁴³ (CPMD) study of MT–Au(111) by Mazzarello et al.²⁰ We intend to reproduce the dynamical behavior of gold atoms observed in that study, but on a larger scale. Thus, we sampled a 14 ps-long CPMD simulation every 0.25 ps, which resulted in a total of 56 atomic configurations of MT adsorbed on a Au(111) surface at saturation coverage ($\theta = 1/3$ ML). DFT calculations were later performed on each configuration using the Quantum Espresso package,⁴⁴ which provides the total energy of the system as well as the Hellmann–Feynman forces on all the atoms of the system. Gradient corrected functionals were used to describe the exchange correlations. The core electrons were described by norm conserving pseudopotentials. The electronic wave functions were expanded using a plane wave basis with an energy cutoff of 45 Ryd. The MT–Au(111) slab considered has four Au layers each having 12 atoms and four MT molecules adsorbed on top of the surface, and periodic boundary conditions were imposed in the plane of the surface.

The set of force field parameters, $\{\chi\}$, is obtained by matching the classical and ab initio forces and energy differences between configurations. Namely, the force field is parametrized through minimization, with respect to the parameters, of the function:³⁹

$$\Gamma(\{\chi\}) = x_F \Delta F + x_U \Delta U \quad (1)$$

where

$$\Delta F^2 = \frac{\sum_{\eta=1}^{n_c} \sum_{i=1}^{N_a} \sum_{k=x,y,z} (F_{i,k}^{cl,\eta} - F_{i,k}^{ai,\eta})^2}{\sum_{\eta=1}^{n_c} \sum_{i=1}^{N_a} \sum_{k=x,y,z} (F_{i,k}^{ai,\eta})^2} \quad (2)$$

and

$$\Delta U^2 = \frac{\sum_{\eta=1}^{n_c-1} \sum_{\zeta=\eta+1}^{n_c} (\Delta U_{\eta,\zeta}^{cl} - \Delta U_{\eta,\zeta}^{ai})^2}{\sum_{\eta=1}^{n_c-1} \sum_{\zeta=\eta+1}^{n_c} (\Delta U_{\eta,\zeta}^{ai})^2} \quad (3)$$

In these expressions, $F_{i,k}^{cl,\eta}$ and $F_{i,k}^{ai,\eta}$ are respectively the k -th Cartesian component of the classical and ab initio forces on atom i in configuration η . $\Delta U_{\eta,\zeta}^{cl}$ and $\Delta U_{\eta,\zeta}^{ai}$ are the classical and ab initio energy difference between atomic configurations η and ζ . N_a and n_c are the total number of atoms and the total number of configurations included in the fit, respectively. x_F and x_U in eq 1 are the weight factors for ΔF and ΔU respectively (such that $x_F + x_U = 1$), which are introduced in order to account for the fact that ΔF contains much more data than ΔU , and their values are suitably chosen to improve the quality of the fit (typically, $x_F \gg x_U$). Note that the classical forces, $F_{i,k}^{cl,\eta} = F_{i,k}^{cl,\eta}(\{\chi\})$, and energy differences, $\Delta U_{\eta,\zeta}^{cl} = \Delta U_{\eta,\zeta}^{cl}(\{\chi\})$, introduce

the dependence of $\Gamma(\{\chi\})$, the function to minimize, on the set of force field parameters, $\{\chi\}$.

The Au(111) surface is modeled using four atomic layers. The bottom most layer, which represents the bulk gold contribution to the surface behavior, is modeled by a rigid layer whose atoms are labeled as Au_b . The remaining three layers have mobile atoms labeled as Au. The Au_b interact with the mobile Au atoms with an effective potential. To describe Au–Au and Au– Au_b interactions, we chose Gupta potentials, which are suitable to describe metallic interactions. DFT studies of the adsorption of alkanethiolates on Au(111) surface have highlighted the importance of the sulfur–gold coordination number on the adsorption geometry and binding energy.^{34,45–50} Hence, a Gupta potential has been included to appropriately describe the S–Au interaction. The contribution to the total potential energy resulting from all the Gupta interactions is given by

$$U_G = \sum_i (V_i - W_i) \quad (4)$$

with

$$V_i = \frac{1}{2} \sum_{j \neq i} A_{\alpha\beta} \exp \left[-p_{\alpha\beta} \left(\frac{r_{ij}}{r_{\alpha\beta}} - 1 \right) \right] \quad (5)$$

and

$$W_i^2 = \sum_{j \neq i} B_{\alpha\beta} \exp \left[-q_{\alpha\beta} \left(\frac{r_{ij}}{r_{\alpha\beta}} - 1 \right) \right] \quad (6)$$

where i and j run over all atoms in the system that have a density-dependent interaction, with r_{ij} being the distance between atoms i and j , while α and β give their atomic type (S, Au, and Au_b); $A_{\alpha\beta}$, $B_{\alpha\beta}$, $r_{\alpha\beta}$, $p_{\alpha\beta}$, and $q_{\alpha\beta}$ are fitting parameters. V_i is the sum of the pairwise repulsions involving atom i , which accounts for the electron orbital overlapping interactions, and $-W_i$ is the attractive many-body energy that introduces the dependence of the potential on the local density in the vicinity of atom i . While the Gupta potential describes the S–Au interactions, we introduce a truncated harmonic three-body potential to describe the Au–S–C valence angle interactions, which has the form

$$U(\theta) = \frac{k_\theta}{2} (\theta - \theta_0)^2 \exp \left[\frac{-(r_{SAu}^8 + r_{SC}^8)}{\rho^8} \right] \quad (7)$$

where θ is the Au–S–C angle, and r_{SAu} and r_{SC} are respectively the S–Au and S–C distances; the fitting parameters of the three body interaction are k_θ , θ_0 , and ρ . The S–C chemical bond is described using a harmonic potential, $U(r_{SC}) = (k/2)(r_{SC} - r_0)^2$, where k and r_0 are the parameters to fit.

$\Gamma(\{\chi\})$ is minimized using the Hanson–Krogh nonlinear least-squares solver, DQED. The parameters obtained for the Gupta potentials are presented in Table 1, while our parametrization of the Au–S–C three body potential yields

Table 1. Gupta Potentials Parameters

	$A_{\alpha\beta}$ (kcal/mol)	$r_{\alpha\beta}$ (Å)	$p_{\alpha\beta}$	$B_{\alpha\beta}$ (kcal/mol)	$q_{\alpha\beta}$
S–Au	22.22	2.335	8.840	43.75	3.510
Au–Au	6.041	2.884	11.04	30.47	3.667
Au– Au_b	7.675	2.884	9.674	24.49	3.526

$k_\theta = 31.52$ kcal mol^{−1}, $\theta_0 = 101.9$ and $\rho = 2.726$ Å with a cutoff distance of 3.5 Å. For the S–C bond potential, we obtain $k = 305.4$ kcal mol^{−1} and $r_0 = 1.797$ Å. With all these parameters, we obtain $\Delta U = 0.102$ and $\Delta F = 0.154$. It is worth mentioning that the force field described above is the result of an exhaustive search where numerous functional forms and parametrizations were tested using MD simulations. In particular, we have tried different parametrizations of Morse and Lennard-Jones potentials to describe the S–Au interaction, harmonic and screened harmonic three-body potentials for the Au–S–C interaction, and various parametrizations of Sutton–Chen⁵¹ potentials to account for the Au–Au and Au– Au_b metallic interactions.

The pair interactions between methylthiolates and that between methyl groups and gold atoms were not included in the force matching procedure. In the MD simulations, such interactions are described using Lennard-Jones potentials of the following form:

$$U_{LJ}(r) = 4\epsilon \left[\left(\frac{\sigma}{r} \right)^{12} - \left(\frac{\sigma}{r} \right)^6 \right] \quad (8)$$

The parameters for the different Lennard-Jones interactions are obtained from refs 29, 30, and 52 and given in Table 2.

Table 2. Lennard-Jones Parameters^{29,30,52}

	ϵ (kcal/mol)	σ (Å)
S–S	0.397	4.970
S–CH ₃	0.209	3.723
CH ₃ –CH ₃	0.175	3.905
CH ₃ –Au	0.143	3.632

Different parametrizations for the sulfur–sulfur Lennard-Jones potentials are presented in refs 29 and 30; we exhaustively tested the different set of potentials and found that the best performance is obtained for the parameters presented in Table 2.

2.2. MD Simulations Details. In this work, we present molecular dynamics simulations of SAMs of Methylthiolate on a Au(111) surface at saturation coverage. The clean Au(111) surface without adsorbates is also considered. In all cases, we use the same force field described in section 2.1. The simulated gold surface consists of three mobile layers each containing 192 Au atoms, and a fourth layer that contains 192 rigid gold atoms that are labeled Au_b . Since the paper focuses on the interaction between Au(111) and methylthiolates, we assume a flat Au(111) surface, neglecting the complexity associated with the presence of surface reconstructions.

The lateral dimensions of the simulation box in the initial configuration are 39.96 and 34.61 Å. A spherical cutoff at 10 Å is used and full periodic boundary conditions are applied. The dimension of the box in the direction perpendicular to the surface is 30.0 Å, which is long enough so that periodic images in such direction do not interact with each other. Box dimensions are allowed to fluctuate with the pressure coupled to a Berendsen barostat while the temperature is kept constant with a Berendsen thermostat. The MD simulations were carried out using DL_POLY_2 v2.20.⁵³ The equations of motion were integrated using a velocity Verlet algorithm with a time step of 1 fs.

In order to investigate the influence of surface vacancies and adatoms, we have considered different initial configurations of

the system. For the gold surface without adsorbed molecules, five different situations are investigated: $(v0,a0)$, $(v0,a1)$, $(v0,a2)$, $(v1,a0)$ and $(v1,a1)$, where (vi,aj) indicates that in the initial configuration there are i vacancies and j adatoms per each $c(4 \times 2)$ cell (see Figure 1). Namely, there are i/j vacancies/

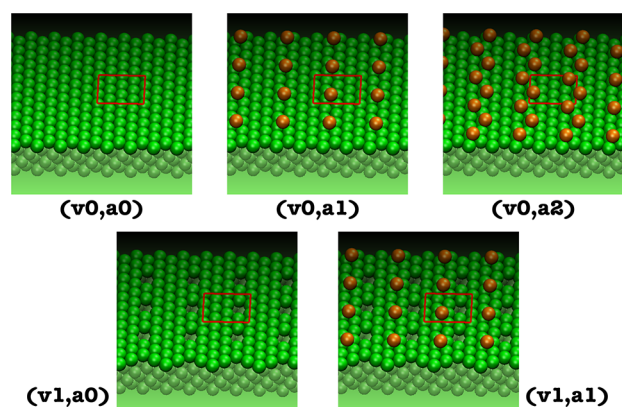


Figure 1. Different initial configurations of the gold surface considered, (vi,aj) , where i and j are respectively the number of vacancies and adatoms (in orange) per $c(4 \times 2)$ cell, which is shown in red.

adatoms every 12 Au atoms of the underneath layer (the $c(4 \times 2)$ contains 12 gold atoms in each atomic layer). Au adatoms are placed above of the topmost Au layer while vacancies are Au atoms missing from that layer. Starting from these configurations, we equilibrate the system at $T = 500$ K for 250 ns. Then, a set of 100 ns equilibration runs are performed where at the end of each run the temperature is decreased by 50 K until $T = 300$ K is reached. After this equilibration process, we observe that all vacancies in $(v1,a0)$ have merged together to form one Au vacancy island, all adatoms in $(v0,a1)$ and $(v0,a2)$ have come together to form one single cluster, and all vacancies in $(v1,a1)$ have been filled by the initial adatoms and thus, this surface is equivalent to $(v0,a0)$. At $T = 300$ K, the simulations started from the equilibrated configuration extend for 500 ns.

For the simulations with MT adsorbed Au(111), the same (vi,aj) combinations described for the clean Au(111) surface are also considered in the initial configuration. To equilibrate the different systems, we adopted two different approaches and choose the one that resulted in a lower energy at the end of the equilibration process. In one approach, we consider initial configurations where a (vi,aj) $c(4 \times 2)$ cell containing 4 MT molecules is repeated across the surface. These atomic configurations are similar to those shown in Figure 1 for the clean Au(111) surface. Then, we repeat the same equilibration procedure as already described for the Au(111) surface without adsorbates. In another approach, we consider initial configurations where the MT molecules are placed on the Au(111) surface that resulted from the equilibration of the clean surface described previously, and then proceed to a similar equilibration of the MT–Au(111) surface. In the initial configuration of both equilibration schemes, the MT molecules are placed equidistributed at ontop positions, but the results are completely independent of the initial placement of the adsorbates. After equilibration of the different MT–Au(111) surfaces, the simulations at 300 K are extended for 250 ns.

2.3. Potential Energy Landscape. Using our force field, we performed structural relaxation of MT–Au(111) surfaces where different adsorption sites for MT on Au(111) were

considered. The MT–Au(111) surfaces contain the same number of atoms and are identical to those described in section 2.2. The adsorption energy with respect to the clean Au(111) surface, and the geometries of various relaxed structures are tabulated in Table 3. The results obtained for the hollow, bridge and ontop sites compare very well with previous DFT results at finite electronic temperature.^{20,54,55}

Table 3. Adsorption Energy (E_a) per MT, S–Au Distance, and S–C Distance and Tilt Angle with Respect to the Surface Normal, of the Various Binding Sites for MT on Au(111)

structure	E_a /MT (eV)	S–Au distance (Å)	S–C distance (Å)	tilt angle (deg)
bridge	−1.72	2.45	1.80	53.4
hollow	−1.57	2.55	1.81	46.8
ontop	−1.52	2.31	1.79	61.1

When adatoms or vacancies are included on the surface, there is an increase of the adsorption energy. Our force field does not reproduce the energetic stability of the MT–Au–MT motif found in other studies.^{19,22} We have also calculated the formation energies of an isolated vacancy, an adatom and a vacancy–adatom pair on both Au(111) and MT–Au(111) surfaces with respect to the clean gold surface and the bridge configuration, respectively. The results are presented in Table 4. Relative to the clean gold surface, the presence of any of such

Table 4. Formation Energies, ΔE , of Different Isolated Defects on the Clean Au(111) and the Bridge MT–Au(111) Surfaces

motif	ΔE Au(111) (eV)	ΔE MT–Au(111)(eV)
1 vacancy	0.49	0.44
1 adatom	0.66	0.37
1 adatom + vacancy	1.14	0.80

defects is energetically more favorable in the SAM, according to the table. At 500 K our MD simulations show the generation of adatoms, which raise from the top atomic layer and leave a monatomic vacancy on it; we will discuss this finding in section 3.

The final configurations of all the surfaces considered in this section, as well as more information on the potential energy landscape of our force field, are provided in the Supporting Information.

2.4. Surface Structures. In this section, we describe the structures of both the Au(111) and the MT–Au(111) surfaces obtained with our MD simulations at 300 K. There are no defects on either surface (i.e., $(v0,a0)$ conditions), which corresponds to the most energetically favorable situations as will be shown in section 3.

Figure 2 shows Au–Au coordination number and its first derivative for the clean Au(111) surface. The cumulative A–B coordination number of two arbitrary species A and B, $cn(r)$, is the average total number of neighboring B atoms contained within a distance r from a central A atom. Its derivative with respect to the A–B distance, $cn'(r)$, is another quantity worth looking at, because it displays a local maximum at the most likely distance between n th A–B neighbors. We see that our force field reproduces the correct structure of gold with a first neighbor distance of 2.87 Å, which increases to 2.88 Å when

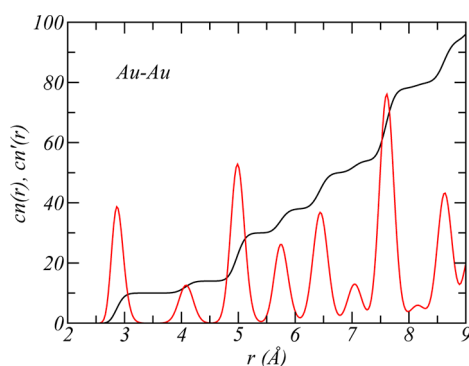


Figure 2. Au–Au coordination number and its first derivative for the Au(111) surface without adsorbates at $T = 300$ K.

thiols are adsorbed, lattice constant 4.08 \AA , and coordination number equal to 10 (the surface-most and the bottom layer atoms have coordination number 8 instead of 12 as that of the two middle atomic layers).

Let us now look into the adsorption of MT molecules on Au(111) surface. The $\sqrt{3}$ hexagonal lattice, characterized by a distance of $\sim 5 \text{ \AA}$ between six-coordinated sulfurs, is recovered for the MT–Au(111) surface, as can be seen in Figure 3A. Figure 3B shows the S–Au coordination number and its derivative for the MT–Au(111) surface. We found that at $1/3$ ML coverage, the S atoms occupy two-coordinated bridge sites with bond distance $r_{\text{SAu}} \approx 2.44 \text{ \AA}$.

3. RESULTS

In this section, we present the results of our simulations of clean Au(111) and MT–Au(111) surfaces. We are interested in comparing surfaces containing different number of adatoms or vacancies. However, the chemical potential of Au atoms is the same for all of the different surfaces considered because each of them is in contact with a bulk crystal that acts as a reservoir of gold atoms. Therefore, we define the excess surface energy, relative to the bulk, as (see Supporting Information):

$$\gamma_S = \frac{1}{A}(E - E_{\text{Au}}N_{\text{Au}}) \quad (9)$$

where N_{Au} is the number of Au atoms in the slab of area A , and E is the total slab energy. E_{Au} is the bulk energy per Au atom that can be calculated through MD simulations of bulk gold. Alternatively, if several surface simulations with different numbers of gold atoms are performed, E_{Au} is given by the slope of the linear relation between E and N_{Au} that follows from eq 9, whose y-intercept is $\gamma_S A$.

We now begin describing the results for clean Au(111) surface (without adsorbates). Panel A of Figure 4 shows the time evolution of the excess surface energy for Au(111) surfaces starting from different initial configurations denoted by (v_i, a_j) , where i and j refer to the number of vacancies and adatoms per $c(4 \times 2)$ cell, respectively (see section 2.2). All (v_i, a_j) simulations presented in Figure 4A were previously equilibrated at high temperature and then slowly cooled down, as described in section 2.2, before the start of the simulation at $T = 300$ K. No new vacancies or adatoms were observed in any of the different simulations. In the (v_1, a_0) surface, all vacancies, initially distributed equally across the simulation cell, merge to form a larger Au vacancy island while the adatoms of the (v_0, a_1) and (v_0, a_2) surfaces cluster to form an incomplete Au(111) layer that covers $1/12$ and $1/6$ of the surface, respectively. The lowest γ_S corresponds to the (v_0, a_0) case indicating that adatoms and vacancies are not energetically favorable at room temperature for the clean Au(111) surface.

Next, we analyze the structure and dynamics of MT–Au(111) surfaces corresponding to the various (v_i, a_j) initial conditions considered. When the initial atomic configuration of the surface contains adatoms or vacancies, they are equidistributed across the surface before starting the simulation. As for the clean Au surface containing vacancies or adatoms, we found that after system equilibration vacancies merge forming a Au vacancy island and adatoms group to form clusters that are incomplete (111) layers. The gold cluster resulting from the (v_0, a_2) MD simulation covers $1/6$ of the surface, while that of the (v_0, a_1) covers $1/12$ of it. STM measurements on the SAMs of alkanethiols on Au(111) have also revealed similar merging of the adatoms and vacancies.¹⁰ The vacancies are monatomic in depths and merge to give larger vacancy islands while adatoms merge to form step edges.¹⁰ The $\sqrt{3}$ cell is obtained for all cases although the adatoms and the vacancies increase the disorder of the surface which can be observed in a more liquid-like S–S $cn'(r)$ (results not shown).

Figure 4B shows the time evolution of the excess surface energy for the different MT–Au(111) surfaces. As we found for the clean gold surface, the (v_0, a_0) surface is still the lowest excess energy surface. DFT calculations by Molina et al.²³ suggest that a $\sqrt{3}$ unit cell containing a single vacancy is energetically favorable for the MT–Au(111) surface at saturation coverage. For the same surface coverage, Grönbeck et al.¹⁹ showed with ab initio simulations that a $c(4 \times 2)$ unit cell having two adatoms and no vacancies has the lowest energy. The DFT and DFT–MD calculations by Wang et al.²² and Mazzarello et al.,²⁰ on the other hand, showed a $c(4 \times 2)$

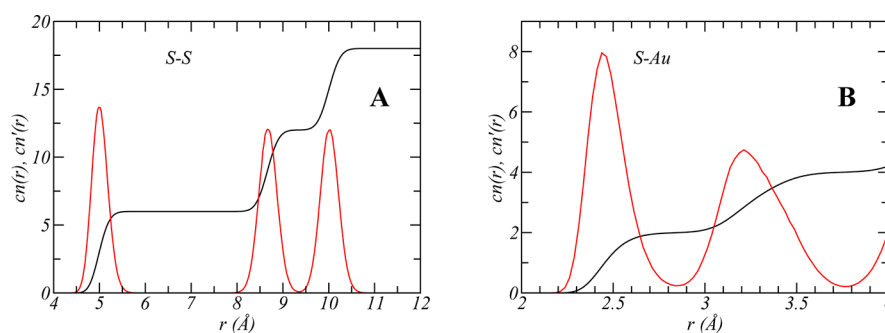


Figure 3. S–S (A) and S–Au (B) coordination numbers and first derivatives for MT adsorbed on the Au(111) surface at $1/3$ ML surface coverage and $T = 300$ K.

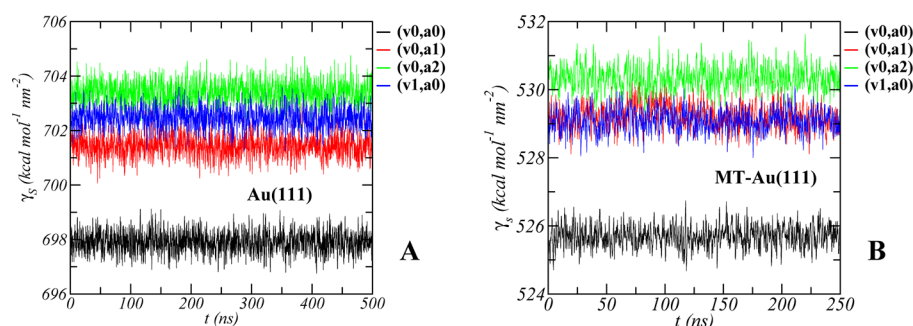


Figure 4. Excess surface energy per unit area, γ_s , for different Au(111) (A) and MT–Au(111) (B) surfaces at $T = 300$ K. The panels show running averages every 10 ps. The labels (v_i, a_j) refer to the number of vacancies and adatoms, per $c(4 \times 2)$ cell, in the initial configuration of the MD simulation.

lattice containing one surface vacancy and an adatom configuration to be energetically the most stable. In this work, we have considered different unit cells in the initial configurations, which contain 16 equiv $c(4 \times 2)$ cells. We observe the adatoms to form clusters and the vacancies to coarsen breaking the initial symmetry of the surface. This difference (as opposed to the DFT simulations) makes it difficult to compare the relative stability of the different adatom/vacancy configurations with the previous DFT studies. It is important to mention that the adatom clustering and vacancy coarsening occurs during a long equilibration process at high temperature. On the other hand, if we do not perform such equilibration, at room temperature the process is much more saddle: the clustering of adatoms and merging of vacancies are not completed after several hundreds of nanoseconds and the different γ_s are higher than those shown in Figure 4B.

Typical structures observed during the simulations of the different MT–Au(111) surfaces are shown in Figure 5. In

experimental technique to characterize surfaces. Figure 6 shows the X-ray reflectivity of the different MT–Au(111) surfaces as

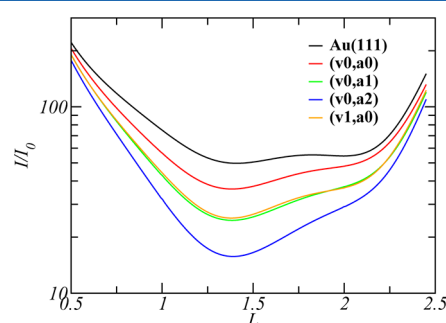


Figure 6. X-ray reflectivity in arbitrary units as a function of the perpendicular momentum transfer, L , in units of $(2\pi)/c$ with $c = 7.06$ Å. The intensity of the Au(111) surface without adsorbates and that of different MT–Au(111) surfaces, which are labeled (v_i, a_j) , at 1/3 ML coverage are presented.

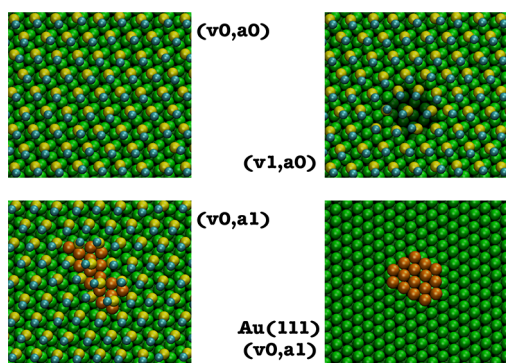


Figure 5. Snapshots representing typical configurations of the MD simulations of different Au(111) and MT–Au(111) surfaces considered at $T = 300$ K. Au adatoms are shown in orange.

particular, we compare the adatom clusters for the $(v0, a1)$ Au(111) and MT–Au(111) surfaces. For the clean Au(111) surface, the adatom clusters of $(v0, a1)$ and $(v0, a2)$ tend to be hexagonal as opposed to the distorted structures observed for the MT–Au(111) surfaces. In addition, the $(v1, a0)$ vacancy island is also hexagonal in the clean Au(111) surface and though it is more deformed for the MT–Au(111) surface, this effect is less significant than for the cluster of adatoms.

In this work, we are particularly concerned with describing the behavior of the very layer of atoms composing the SAM surface. Grazing incidence X-ray diffraction is a powerful

compared to the surface without thiols adsorbed (see Supporting Information). The rod-scans shown in the Figure are time averages over the 250 ns MD simulations presented in Figure 4B. We found that the experimentally observed drop in intensity after MT adsorption on the Au(111) surface²⁰ cannot be accounted for when no defects are present as it is the case of the $(v0, a0)$ surface. The magnitude of the experimental intensity drop, however, is consistent with that of the surface containing small adatom clusters and with that calculated for the surface having vacancy islands, viz. $(v0, a1)$ and $(v1, a0)$ configurations. A larger cluster size, however, such as that of $(v0, a2)$ results in a decrease of the X-ray intensity that is much larger than that reported experimentally.

An important and intriguing question in context of the MT–Au(111) surfaces is related to the source of adatoms and vacancies. Where as the DFT calculations and GIXRD of Mazzarello et al.²⁰ clearly state generation of the adatoms from the top layer of the slab as a result of the S–Au interaction, there are also STM experiments that report that the adatom may be coming from the bulk.¹⁸ In our simulations, we did not observe the production of new adatoms in any of the different cases at room temperature. During simulations at $T = 500$ K, however, Au adatoms that raise from the surface leaving a vacancy on it are frequently observed. For the $(v0, a0)$ surface, many events of adatom generation occur during the 250 ns simulation at that temperature; after raising from the underneath Au atomic layer, such gold adatoms diffuse across

the Au(111) layer. While adatoms diffuse on the Au(111) surface, they can encounter a vacancy left by another adatom or by itself and fill it. Therefore, the total number of adatoms on the surface is not a monotonic function of time in our MD simulations. We observe up to three adatoms at the same time in our simulation cell where the underlying Au atomic layer contains 192 atoms if completely filled.

Figure 7 shows a typical configuration of the MT–Au(111) surface at 500 K, starting from (v0,a0) conditions. Adatoms are

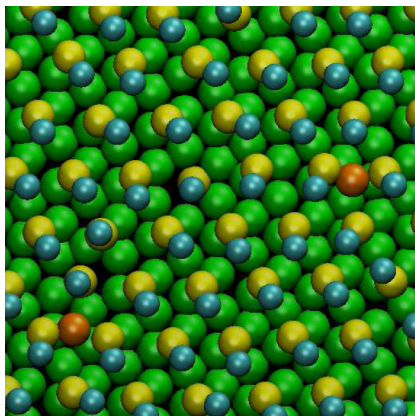


Figure 7. Snapshot of a MD simulation at 500 K starting from a (v0,a0) configuration at saturation coverage. The snapshot shows adatoms (orange) that are pulled from the Au(111) surface leaving vacancies.

also observed at 500 K for the MT–Au(111) surfaces with (v0,a1) and (v1,a0) initial conditions. In the first case, newly generated adatoms diffuse until they join the cluster of adatoms on the surface and vacancies are left. In the second case, on the other hand, adatoms are generated frequently creating new surface vacancies but these Au adatoms are short-lived and return to the surface (generally falling into the vacancy island) typically within the nanosecond time scale.

Finally, we are interested in quantifying the diffusion of adatoms in the SAM as compared to the clean gold surface. Therefore, we consider the case where a single adatom is added to the (v0,a0) Au(111) and MT–Au(111) surfaces. In two dimensions, the diffusion coefficient of the adatom, D_a , can be obtained using the relationship $\langle r_a^2 \rangle = 4D_a t$, where $\langle r_a^2 \rangle$ is the mean square displacement of the adatom on the surface. Using 50 ns-long simulations to calculate $\langle r_a^2 \rangle$, we obtained $D_a = 2.7 \times 10^{-5} \text{ cm}^2 \text{ s}^{-1}$ and $D_a = 6.7 \times 10^{-6} \text{ cm}^2 \text{ s}^{-1}$ at 300 K for the adatom on the Au(111) and the MT–Au(111) surfaces, respectively. In the last case, the sulfur–adatom coordination number is equal to 2, and the adatom diffuses by hopping between different pairs of sulfurs to which it is temporarily bound.

4. CONCLUSION

In summary, we studied the surface behavior of SAMs of MT on Au(111) using classical MD simulations. We developed a new force field that was parametrized through a force matching procedure starting from ab initio calculations. This force field was able to reproduce the $(\sqrt{3} \times \sqrt{3})R30$ lattice found experimentally for the saturation coverage adsorption of sulfur atom^{56,57} and MT with and without adatoms or vacancies. For room temperature simulations, the lowest energy monolayer, relative to the bulk, is that which contains no defects and where

the MT–molecule sulfur occupies, on average, a two coordinated bonding site on the Au(111) surface. This absorption site has been suggested to be preferred by many DFT studies.^{46,47,49} To the best of our knowledge, however, this is the first study to find the same result at room temperature and considering the dynamics of the system within the hundreds of nanoseconds time scale. MT adsorption reduces the energy required for vacancy or adatom formation as compared to the clean Au(111) surface. When Au vacancies are included in the surface simulation, they coarsen to form a larger gold vacancy island. These monatomic Au vacancy islands for SAMs of thiols on gold(111) that can be experimentally observed by STM experiments are believed to occur during alkanethiolate chemisorption.^{17,27,58} In agreement with experimental results,²⁸ we have found that these islands are also uniformly covered by thiols. On the other hand, when adatoms are included in the MD simulation, they come into contact and form clusters that are hexagonal in the Au(111) surface and more distorted in the MT–Au(111). This result is consistent with the STM experiments of Ohgi et al.,⁵⁹ who observed that Au atoms deposited on top of a thiol SAM penetrate through it to form monatomic-height gold clusters underneath the SAM on the Au(111) surface. They also found that these clusters become larger as more Au atoms are deposited on the surface. Small clusters or vacancy islands covering each 1/12 ML can account for the magnitude of the drop in intensity experimentally observed in X-ray reflectivity scans,²⁰ taking the Au(111) surface as a reference, without introducing any adjustable parameters.

As for the source of surface Au adatoms in the MT–Au(111) monolayer, we observed in our simulations that at elevated temperatures, Au atoms from the topmost layer of Au(111) can be raised leaving a surface vacancy. In particular, vacancy islands give the gold lattice the flexibility to promote frequent events of adatom generation, but these adatoms are short-lived and diffuse to fall into the large monatomic void. On the other hand, adatoms raising from the surface near an existing cluster will diffuse to join it within a few nanoseconds. Adatom generation is also observed in regions without defects.

Furthermore, assuming that the density of adatoms is low enough so that adatoms interaction can be neglected, we calculated the diffusion coefficient of gold adatoms in the MT–Au(111) surface without defects to be $D_a = 6.7 \times 10^{-6} \text{ cm}^2 \text{ s}^{-1}$ at room temperature, which is almost an order of magnitude slower than the adatom diffusion in the Au(111) surface without adsorbate at the same temperature, but it still corresponds to a liquid-like diffusion. In the MT–Au(111) SAM, free adatoms diffuse by hopping between pairs of sulfurs to which they are bound for a short period of time. The presence of gold adatoms have been recently suggested in structural models to account for the observed $c(4 \times 2)$ lattice in SAMs of thiols on gold(111).^{18,20–22,24} We set up our initial conditions to study such models but found that due to fast adatom diffusion, a scenario where each $c(4 \times 2)$ cell contains solid-phase adatoms at room temperature is unlikely. A similar scenario occurs for single atom vacancies where we observe the formation of vacancy islands, thus, a unit cell containing solid-phase vacancies is an unlikely situation at room temperature. It is also worth mentioning that we did observe movement of center of mass of adatom clusters and vacancy islands, but their diffusion, however, occurs in a time scale that is far beyond those considered in this study.

The force field developed in this study was able to reproduce several features of SAMs of MT on Au(111) observed experimentally. The MT–MT pair interactions were not included in the fitting procedure, but rather taken from the literature to perform the MD simulations. Our current efforts are concentrated in improving this fact, though we believe the relevance of this should be less significant for thiols with longer chains, where the van der Waals forces are more dominant and these literature parameters are known to properly describe the hydrocarbon layer. We intend to study such long-alkyl chain systems in the near future because they are more interesting from the point of view of potential applications. Although, the classical force field closely matches our DFT energy calculations, it does not reproduce the energetic preference for the MT–Au–MT motif found in other studies^{19,22} at 0 K. This issue will be addressed in future studies. We also tested the transferability of the force field by performing simulations of passivated gold nanoparticles. We are able to reproduce some of the known structures of gold clusters of different small sizes which suggests that, though this force was developed from first-principle calculations for slab models, nevertheless, it could be applied to other geometries. We also target to model large thiol passivated Au nanoparticles.

■ ASSOCIATED CONTENT

■ Supporting Information

Comparison of DFT and classical energies, details concerning the calculation of the surface energy, further information on the potential energy landscape and the method used to obtain the results shown in section 2.3, and a thorough description of the methodology used to calculate the GIXRD rod-scans. This material is available free of charge via the Internet at <http://pubs.acs.org/>.

■ AUTHOR INFORMATION

Corresponding Author

*E-mail: (G.S.L.) longogs@northwestern.edu; (S.S.) scandolo@ictp.it.

Notes

The authors declare no competing financial interest.

■ ACKNOWLEDGMENTS

The authors thank S.I.S.S.A for support during the initial stages of this work. We also thank Prof. R. Mazzarello and Prof. R. Rousseau their valuable help. G.S.L. thanks the postdoctoral fellowship support from the National Science Foundation Grant DMR-0520513 of the Materials Research Science and Engineering Center Program at Northwestern University. He also thanks Prof. M. Olvera de la Cruz and Prof. I. Szleifer.

■ REFERENCES

- (1) Chaki, N. K.; Vijayamohan, K. *Biosens. Bioelectron.* **2002**, *17*, 1–12.
- (2) Love, J. C.; Estroff, L. A.; Kriebel, J. K.; Nuzzo, R. G.; Whitesides, G. M. *Chem. Rev.* **2005**, *105*, 1103–1170.
- (3) Akkerman, H. B.; Blom, P. W. M.; de Leeuw, D. M.; de Boer, B. *Nature* **2006**, *441*, 69–72.
- (4) Poirier, G. E.; Tarlov, M. J. *Langmuir* **1994**, *10*, 2853–2856.
- (5) Poirier, G. E.; Pylant, E. D. *Science* **1996**, *272*, 1145–1148.
- (6) Schreiber, F. *Prog. Surf. Sci.* **2000**, *65*, 151–257.
- (7) Widrig, C. A.; Alves, C. A.; Porter, M. D. *J. Am. Chem. Soc.* **1991**, *113*, 2805–2810.
- (8) Yamada, R.; Uosaki, K. *Langmuir* **1998**, *33*, 855–861.
- (9) Yamada, R.; Wano, H.; Uosaki, K. *Langmuir* **2000**, *16*, 5523–5525.
- (10) Wano, H.; Uosaki, K. *Langmuir* **2005**, *21*, 4024–4033.
- (11) Alves, C. A.; Smith, E. L.; Porter, M. D. *J. Am. Chem. Soc.* **1992**, *114*, 1222–1227.
- (12) Camillone, N.; Chidsey, C. E. D.; Liu, G.; Scoles, G. *J. Chem. Phys.* **1993**, *98*, 3503–3511.
- (13) Schwartz, P.; Schreiber, F.; Eisenberger, P.; Scoles, G. *Surf. Sci.* **1999**, *423*, 208–224.
- (14) Delamarche, E.; Michel, B.; Gerber, C.; Anselmetti, D.; Guentherodt, H. J.; Wolf, H.; Ringsdorf, H. *Langmuir* **1994**, *10*, 2869–2871.
- (15) Fenter, P.; Eberhardt, A.; Liang, K. S.; Eisenberger, P. *J. Chem. Phys.* **1997**, *106*, 1600–1608.
- (16) Danisman, M. F.; Casalis, L.; Bracco, G.; Scoles, G. *J. Phys. Chem. B* **2002**, *106*, 11771–11777.
- (17) Dishner, M. H.; Hemminger, J. C.; Feher, F. J. *Langmuir* **1997**, *13*, 2318–2322.
- (18) Maksymovych, P.; Sorescu, D. C.; Yates, J. T. *Phys. Rev. Lett.* **2006**, *97*, 146103.
- (19) Grönbeck, H.; Häkkinen, H.; Whetten, R. L. *J. Phys. Chem. C* **2008**, *112*, 15940–15942.
- (20) Mazzarello, R.; Cossaro, A.; Verdini, A.; Rousseau, R.; Casalis, L.; Danisman, M. F.; Floreano, L.; Scandolo, S.; Morgante, A.; Scoles, G. *Phys. Rev. Lett.* **2007**, *98* (016102), 1–4.
- (21) Cossaro, A.; Mazzarello, R.; Rousseau, R.; Casalis, L.; Verdini, A.; Kohlmeier, A.; Floreano, L.; Scandolo, S.; Morgante, A.; Klein, M. L.; Scoles, G. *Science* **2008**, *321*, 943–946.
- (22) Wang, J.-G.; Selloni, A. *J. Phys. Chem. C* **2007**, *111*, 12149–12151.
- (23) Molina, L. M.; Hammer, B. *Chem. Phys. Lett.* **2002**, *360*, 264–271.
- (24) Torres, E.; Blumenau, A. T.; Biedermann, P. U. *Phys. Rev. B* **2009**, *79* (075440), 1–6.
- (25) Edinger, K.; Goelzhaeuser, A.; Demota, K.; Woell, C.; Grunze, M. *Langmuir* **1993**, *9*, 4–8.
- (26) Cavalleri, O.; Hirstein, A.; Kern, K. *Surf. Sci.* **1995**, *340*, L960–L964.
- (27) Poirier, G. E. *Langmuir* **1997**, *13*, 2019–2026.
- (28) Poirier, G. E. *Chem. Rev.* **1997**, *97*, 1117–1128.
- (29) Hautman, J.; Klein, M. L. *J. Chem. Phys.* **1989**, *91*, 4994–5001.
- (30) Siepmann, J. I.; McDonald, I. R. *Langmuir* **1993**, *9*, 2351–2355.
- (31) Mar, W.; Klein, M. L. *Langmuir* **1994**, *10*, 188–196.
- (32) Pertsin, A. J.; Grunze, M. *Langmuir* **1994**, *10*, 3668–3674.
- (33) Bhatia, R.; Garrison, B. J. *Langmuir* **1997**, *13*, 4038–4043.
- (34) Beardmore, K. M.; Kress, J. D.; Grönbeck-Jensen, N.; Bishop, A. R. *Chem. Phys. Lett.* **1998**, *286*, 40–45.
- (35) Liu, K. S. S.; Yong, C. W.; Garrison, B. J.; Vickerman, J. C. *J. Phys. Chem. B* **1999**, *103*, 3195–3205.
- (36) Zhang, L.; Goddard, W. A.; Jiang, S. J. *Chem. Phys.* **2002**, *117*, 7342–7349.
- (37) Olmos-Asar, J. A.; Rapallo, A.; Mariscal, M. M. *Phys. Chem. Chem. Phys.* **2011**, *13*, 6500–6506.
- (38) Ercolessi, F.; Adams, J. B. *Europhys. Lett.* **1994**, *26*, 583–588.
- (39) Tangney, P.; Scandolo, S. J. *Chem. Phys.* **2002**, *117*, 8898–8904.
- (40) Izvekov, S.; Parrinello, M.; Burnham, C. J.; Voth, G. A. *J. Chem. Phys.* **2004**, *120*, 10896–10913.
- (41) Youngs, T. G. A.; Del Pópolo, M. G.; Kohanoff, J. *J. Phys. Chem. B* **2006**, *110*, 5697–5707.
- (42) Izvekov, S.; Voth, G. A. *J. Phys. Chem. B* **2005**, *109*, 2469–2473.
- (43) Car, R.; Parrinello, M. *Phys. Rev. Lett.* **1985**, *55*, 2471–2474.
- (44) Giannozzi, P.; et al. *J. Phys.: Condens. Matter* **2009**, *21* (395502), 1–19.
- (45) Grönbeck, H.; Curioni, A.; Andreoni, W. *J. Am. Chem. Soc.* **2000**, *122*, 3839–3842.
- (46) Hayashi, T.; Morikawa, Y.; Nozoye, H. *J. Chem. Phys.* **2001**, *114*, 7615–7621.
- (47) Akinaga, Y.; Nakajima, T.; Hirao, K. *J. Chem. Phys.* **2001**, *114*, 8555–8564.

- (48) Vargas, M. C.; Giannozzi, P.; Selloni, A.; Scoles, G. *J. Phys. Chem. B* **2001**, *105*, 9509–9513.
- (49) Gottschalck, J.; Hammer, B. *J. Chem. Phys.* **2002**, *116*, 784–790.
- (50) Yourdshahyan, Y.; Rappe, A. M. *J. Chem. Phys.* **2002**, *117*, 825–833.
- (51) Sutton, A. P.; Chen, J. *Philos. Mag. Lett.* **1990**, *61*, 139–146.
- (52) Mahaffy, R.; Bhatia, R.; Garrison, B. J. *J. Phys. Chem. B* **1997**, *101*, 771–773.
- (53) Smith, W.; Forester, T. R.; Todorov, I. T. *The DL_POLY_2 user manual*; Daresbury Laboratory: Daresbury, U.K., 2009.
- (54) Rousseau, R.; Mazzarello, R.; Scandolo, S. *ChemPhysChem* **2005**, *6*, 1756–1760.
- (55) Rousseau, R.; De Renzi, V.; Mazzarello, R.; Marchetto, D.; Biagi, R.; Scandolo, S.; del Pennino, U. *J. Phys. Chem. B* **2006**, *110*, 10862–10872.
- (56) Vericat, C.; Andreasen, G.; Vela, M. E.; Salvarezza, R. C. *J. Phys. Chem. B* **1999**, *104*, 302–307.
- (57) Vericat, C.; Vela, M. E.; Andreasen, G. A.; Salvarezza, R. C.; Borgatti, F.; Felici, R.; Lee, T. L.; Renner, F.; Zegenhagen, J.; Martin-Gago, J. A. *Phys. Rev. Lett.* **2003**, *90*, 075506.
- (58) Vericat, C.; Vela, M. E.; Benitez, G. A.; Martin Gago, J. A.; Torrelles, X.; Salvarezza, R. C. *J. Phys.: Condens. Matter* **2006**, *18*, R867–R900.
- (59) Ohgi, T.; Sheng, H.-Y.; Dong, Z.-C.; Nejo, H. *Surf. Sci.* **1999**, *442*, 277–282.